

## ARTICLE OPEN



# Anthropogenic impact on the severity of compound extreme high temperature and drought/rain events in China

Wanling Li , Bo Sun <sup>1,2,3</sup>✉, Huijun Wang <sup>1,2,3</sup>, Botao Zhou , Huixin Li <sup>1,2,3</sup>, Rufan Xue , Mingkeng Duan <sup>1,2</sup>, Xiaochun Luo <sup>4</sup> and Wenwen Ai <sup>4</sup>

Compared with individual extreme events, compound events have more severe impacts on humans and the natural environment. This study explores the change in severity of compound extreme high temperature and drought/rain events (CHTDE/CHTRE) and associated influencing factors. The CHTDE and CHTRE intensified in most areas of China in summer (June–July August) during 1961–2014. Under global warming, the increased water-holding capacity of the atmosphere and the decreased relative humidity led to an increase in the severity of CHTDE. The severity of CHTRE is increased because of enhanced transient water vapor convergence and convective motion. Anthropogenic climate change, especially greenhouse gas forcing, which contributes 90% to the linear change in the severity of CHTDE and CHTRE, is identified as the dominant factor affecting the severity of CHTDE in China. In addition, the historical natural forcing (hist-NAT) may be related to the interannual-to-decadal variability in the severity of CHTDE/CHTRE.

*npj Climate and Atmospheric Science* (2023)6:79; <https://doi.org/10.1038/s41612-023-00413-3>

## INTRODUCTION

Over recent years, extreme precipitation events, extreme drought events, extreme high temperature events and extreme storm events have occurred frequently and have had devastating impacts on human life and the ecological environment in many places<sup>1–4</sup>. For example, 38.305 million people were affected by the extreme high temperature event in China during the summer of 2022<sup>5</sup>. In the summer of 2021, China experienced many extreme rainfall events, each of which caused property losses of approximately US\$12 billion<sup>6</sup>. Furthermore, the Lancet Countdown Regional Centre in Asia reported that hundreds to thousands of people lose their lives in extreme floods each year in China, and millions to tens of millions of people cannot drink water because of extreme droughts<sup>7</sup>. In particular, in the context of global warming, compound extreme weather and climate events, which are multivariate extremes at multiple temporal and spatial scales that can further exacerbate the risks and effects of individual extreme events, have become more frequent. Compound extreme events have great impacts on crops, grassland ecosystems and vegetation<sup>3,8–10</sup>. Thus, climate change has become one of the most severe challenges facing humankind. Attaching great importance to the change in different types of compound extreme events and research it is the key to preventing and mitigating natural disasters and ensuring economic development and human happiness.

Since the Intergovernmental Panel on Climate Change Special Report on Climate Extremes (IPCC SREX) first explicitly proposed the conception of compound extreme events in 2012<sup>11</sup>, the definition of compound extreme events has been continuously enriched and expanded<sup>3,12</sup>. For compound extreme high temperature and drought/rain events (CHTDE and CHTRE), the quantitative identification methods can be classified into three categories<sup>12–14</sup>. One category is that the concurrent extremes of

different variables should be greater than or less than their specified extreme thresholds<sup>15–17</sup>. Another category is to recognize compound events based on empirical statistical models of meteorological indicators such as compound drought and the heat wave magnitude index<sup>8,18–20</sup>. The third category is to implement the probability statistic indicator based on joint distributions of multiple single-event indicators. In this category, the effects of dependence and interaction between multiple extreme driving factors and compound extreme events are investigated<sup>14,21,22</sup>. The Standardized Compound Event Indicator developed from the Standardized Precipitation Index (SPI) and Standardized Temperature Index are good examples of this category<sup>23</sup>. However, most of these indicators are obtained based on data at the monthly time scale, whereas the variation at the daily time scale is smoothed out. In addition, the interaction between different time scales and physical meteorological elements is not well considered, and the extreme degree of compound events is not well quantified at present<sup>13,24</sup>.

Increasing attention has been given to CHTDE in recent years. The IPCC AR6<sup>3</sup> report indicates that the occurrence probability of CHTDE has been increasing at the global scale since the 1950s, and the frequency and intensity of CHTDE have increased with high confidence. Wang *et al.*<sup>25</sup> investigated the spatiotemporal changes in CHTDE over global land using SPI and the copula method. They demonstrated that the significant increase in the probability of CHTDE depends on the increase in the negative correlation between temperature and SPI. In China, monthly CHTDE shows a significant increasing trend, especially in Northeast China, where the occurrence probability of CHTDE has increased by 0.05 per decade<sup>26–28</sup>. In addition, the continuous and stable high-pressure system anomaly is conducive to the formation of downdrafts and low-level thermal anomalies, which can effectively reduce cloud cover and increase solar radiation. As

<sup>1</sup>Collaborative Innovation Center on Forecast and Evaluation of Meteorological Disasters/Key Laboratory of Meteorological Disasters, Ministry of Education/Joint International Research Laboratory of Climate and Environment Change, Nanjing University of Information Science and Technology, Nanjing, China. <sup>2</sup>Southern Marine Science and Engineering Guangdong Laboratory, Zhuhai, China. <sup>3</sup>Nansen Zhu International Research Centre, Institute of Atmospheric Physics, Chinese Academy of Sciences, Beijing, China.

<sup>4</sup>Meteorological Service Center of Jiangsu Province, Nanjing, China. ✉email: sunb@nuist.edu.cn

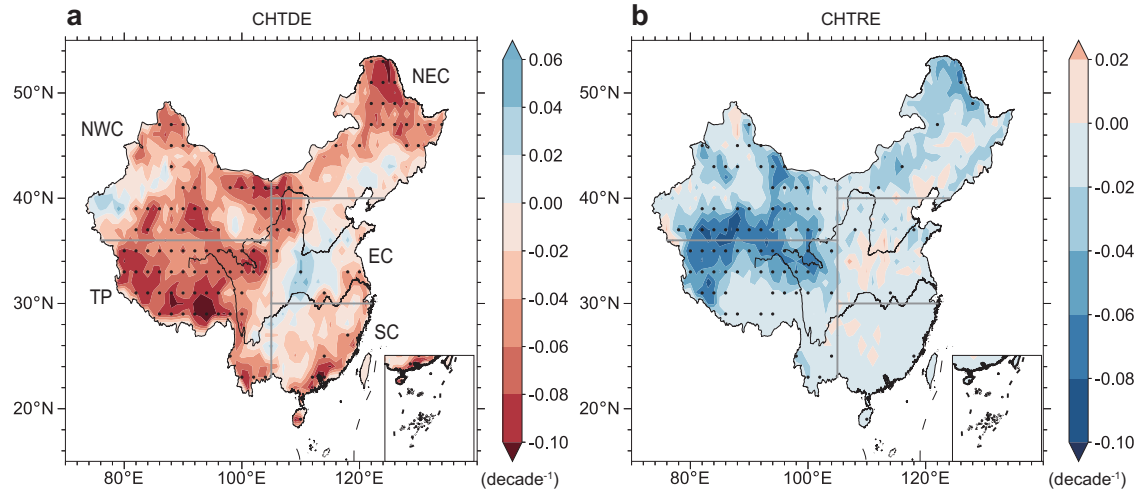


**Fig. 1 Linear trends of CHTDEI and CHTREI.** Observed linear trends of (a) CHTDEI and (b) CHTREI based on CN05.1 in the summers from 1961 to 2014 (units:  $\text{decade}^{-1}$ ) over China. The dotted area indicates that the linear trend is significant at the 95% confidence level. The five subregions of China are shown in (a), including Northwest China (NWC), the Tibetan Plateau (TP), Northeast China (NEC), Eastern China (EC) and the coastal region of South China (SC).

a result, CHTDE are intensified in China and display daily variations<sup>10,29,30</sup>. However, few studies have focused on the regional characteristics of CHTDE and reproducibility in the simulations of CHTDE from the Coupled Model Intercomparison Project Phase 6 (CMIP6) on a daily time scale. In addition, compared with the simulations of CHTDE by CMIP5, the performance and uncertainty range of CHTDE by CMIP6 are not well understood.

In addition to CHTDE, CHTRE also has important effects on the environment. When intensified extreme heavy precipitation events occur together with extreme high-temperature events more frequently, a higher frequency of CHTRE can be found in both daytime and nighttime<sup>16</sup>. In addition, it is almost impossible for extreme precipitation events and extreme high-temperature events to occur consecutively within a week in China. However, it has become more likely that a once-in-50-year extreme precipitation event and an extreme high-temperature event occur together within a week in recent decades<sup>31</sup>. However, our understanding of CHTRE is very limited, the mechanism of CHTRE is not clear, and little attention has been given to the study of the severity of CHTRE based on reliable observations and numerical models at present.

To investigate the extent to which climate change is caused by anthropogenic activities, many studies on extreme events have been conducted and confirmed that anthropogenic activities, especially emissions of greenhouse gases, are the main reason for the increase in extreme temperature events, extreme precipitation events and drought events on both regional and global scales<sup>4,32,33</sup>. In recent years, human influence on compound extreme events has gradually attracted more attention. Some studies have found that anthropogenic activities are likely to influence the occurrence frequency and intensity of global CHTDE<sup>26–28,34</sup>. Specifically, under global warming, the influence of excess heat on CHTDE has been larger than that of precipitation deficiency in recent decades<sup>25,35</sup>. However, the understanding of the changes in CHTDE and CHTRE influenced by anthropogenic activities and natural forcings in different regions of China is still less than sufficient.

The present study uses a bivariate joint probability distribution between the total number of days and the maximum duration of compound extreme events and multimodel results of CMIP6 to study the changes and potential causes of the severity of CHTDE and CHTRE over different subregions of China. The relative

contributions of external forcings, including anthropogenic activities and natural variability, to the changes are also explored.

## RESULTS

### Observed changes in CHTDE and CHTRE

In this study, the combined probability of the days and duration of simultaneously occurring high temperature and drought (rain) events were considered, and the severity of the compound event (see Methods) was quantified. Here, smaller CHTDE and CHTRE indexes (CHTDEI/CHTREI) represent a more violent and severe CHTDE/CHTRE. Therefore, a downward trend in CHTDEI/CHTREI indicates an increasing trend in the severity of CHTDE/CHTRE, and vice versa. To determine the optimal fitting copulas for calculating bivariate joint distribution, three criteria were used to compare the performance of different copulas<sup>36,37</sup>. According to the results, the CHTDEI and CHTREI based on Clayton and Gumbel are shown in Fig. 1 (see Methods).

Specifically, according to the linear trend analysis (see Methods), the observed CHTDEI in Northwest China (NWC), Northeast China (NEC), the Tibetan Plateau (TP) and the coastal region of South China (SC) exhibits a statistically significant (at the 95% confidence level) decreasing trend of approximately 0.04 to 0.1 per decade from 1961 to 2014 (Fig. 1a). This means that the severity of CHTDE is increasing significantly during summer in most areas of China except for Eastern China (EC). In contrast, the CHTREI displays a significant decreasing trend of approximately 0.02 to 0.1 per decade in the northern TP and southern NWC (Fig. 1b). The intensified severity of the CHTRE in NWC under the background of increasing warming and humidification deserves more attention<sup>38</sup>. In addition, there is a decreasing trend of approximately 0.02 to 0.06 per decade only in the northern part of NEC. Moreover, the spatial patterns of the observed trends in the severity of CHTDE and CHTRE show that CHTDE and CHTRE increased significantly in areas where the frequencies of CHTDE and CHTRE were higher and the durations tended to be longer (Supplementary Figure 1, Supplementary Figure 2).

### Underlying mechanisms of increased severity of CHTDE and CHTRE

Based on the spatial distribution of the linear trend in CHTDEI and CHTREI over China, we further explored the potential causes of the increased severity of CHTDE and CHTRE.

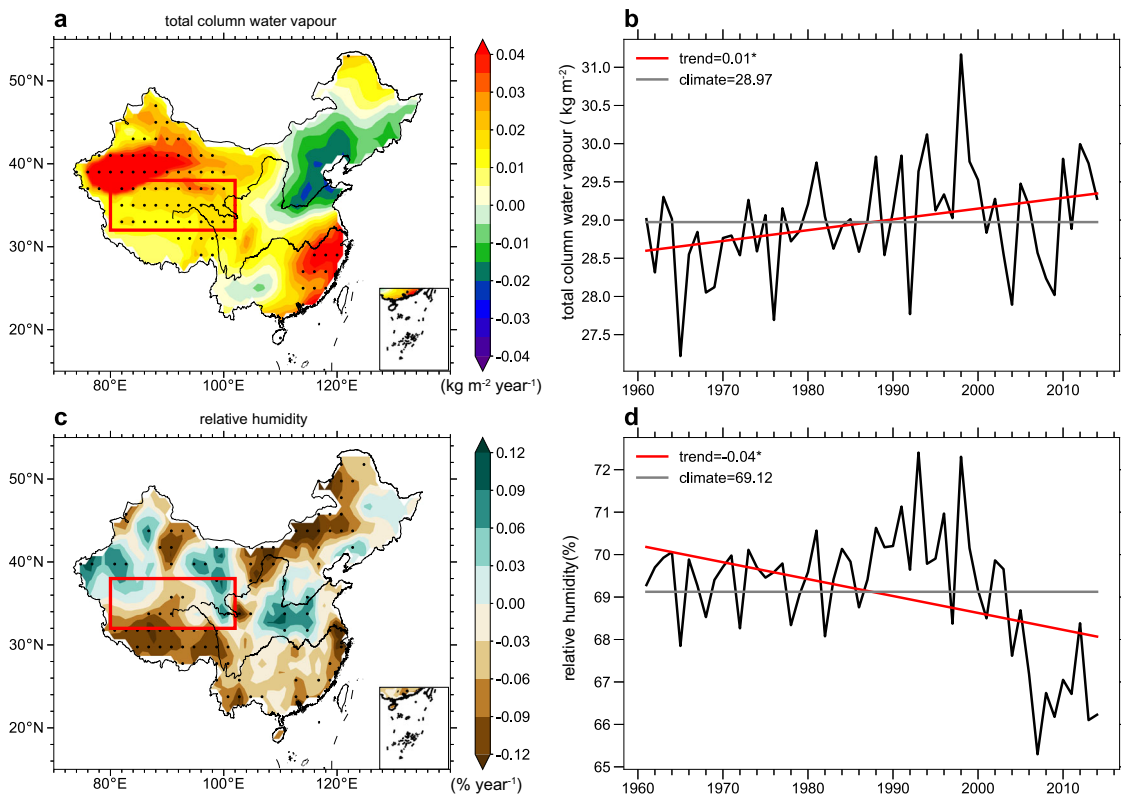


**Fig. 2 Linear trends of total column water vapor and relative humidity.** Spatial distribution of observed linear trends in (a) total column water vapor (units:  $\text{kg m}^{-2} \text{year}^{-1}$ ) and (c) surface relative humidity (units:  $\% \text{year}^{-1}$ ) in the summers from 1961 to 2014 over China; Regional average time series of (b) total column water vapor and (d) surface relative humidity over China in the summers from 1961 to 2014. Dotted area and \* indicate that the linear trend is significant at the 95% confidence level. In (b) and (d), the red line denotes the corresponding linear trend (units:  $\text{kg m}^{-2} \text{year}^{-1}$  for total column water vapor and  $\% \text{year}^{-1}$  for relative humidity) and the gray line denotes the climatology (units:  $\text{kg m}^{-2}$  for total column water vapor and  $\%$  for relative humidity).

According to the Clausius-Clapeyron equation, due to the rapid increase in temperature under global warming, the water vapor content that can be held in the air keeps increasing<sup>38</sup>, leading the saturation water vapor pressure ( $q_s$ ) to increase significantly. Historically, since the increase rate of actual water vapor pressure ( $q$ ) usually increases at a slower rate than the saturation water vapor pressure<sup>39,40</sup>, the ratio between  $q$  and  $q_s$  is generally reduced, so the relative humidity

$$\text{RH} = \frac{q}{q_s} \quad (1)$$

may be decreased. The lower relative humidity is not conducive to water vapor saturation, so it may inhibit precipitation. As shown in Fig. 2, the water vapor content increased over China (Fig. 2a, b), and the relative humidity decreased significantly, especially in the TP (Fig. 2c). In addition, since the beginning of the 21st century, the increased level of black carbon aerosols has caused warming of the middle and upper troposphere and intensification of zonal wind vertical shear in South Asia. This warming and increasing wind shear strengthened the vertical convection and cloud condensation in the atmosphere over South Asia, leading to more water vapor converging over the Indian subcontinent, which is the main external water vapor transport source for precipitation in the TP region<sup>41,42</sup>. Therefore, the water vapor transported to the TP region decreased during summer. With decreased water vapor transport, the relative humidity has decreased dramatically since the 2000s (Fig. 2d), making it more difficult for water vapor to reach saturation over the TP. Hence, less precipitation and severe drought will occur on the TP. In summary, the significant increase in the severity of CHTDE in most areas of China, especially on the

TP, may be largely linked with the decrease in relative humidity under global warming.

The increase in severity of CHTRE is mainly concentrated in western China (Fig. 1b). The climatology and linear trend of the total number of days and maximum duration on CHTRE also indicated that western China was the key area for the intensified CHTRE (Supplementary Figure 2). Therefore, we analyzed the potential mechanism of increased severity of CHTRE in western China (red rectangles in Supplementary Figure 2 and Fig. 3,  $80\text{--}102^\circ\text{E}, 32\text{--}38^\circ\text{N}$ ). The Clausius-Clapeyron rate indicates that the intensity of extreme precipitation increases significantly at higher temperatures with a faster-increasing rate than that of the water-holding capacity of the atmosphere. The response intensity of convective precipitation to atmospheric warming is much greater than that of the Clausius-Clapeyron rate, which could lead to more extreme precipitation events<sup>43</sup>. Thus, when the water-holding capacity of the atmosphere is increased, convective motion triggered by favorable transient motion can cause more extreme precipitation.

The composite differences (Fig. 3) between the relatively warm period (1988–2014) and the relatively cold period (1961–1987) show that transient water vapor transport (Fig. 3c) increased significantly during regional CHTRE events (i.e., CHTRE events occurred in more than 10% of the grid points over western China). The increased transient water vapor transport over western China during the relatively warm period mainly came from the Bay of Bengal. Composite differences in the transient surface wind (Fig. 3d) indicate that the convergence of water vapor flux over western China in the warm period is mainly due to the effect of wind divergence; that is, abnormal transient south winds can transport water vapor from the Bay of Bengal to western China,

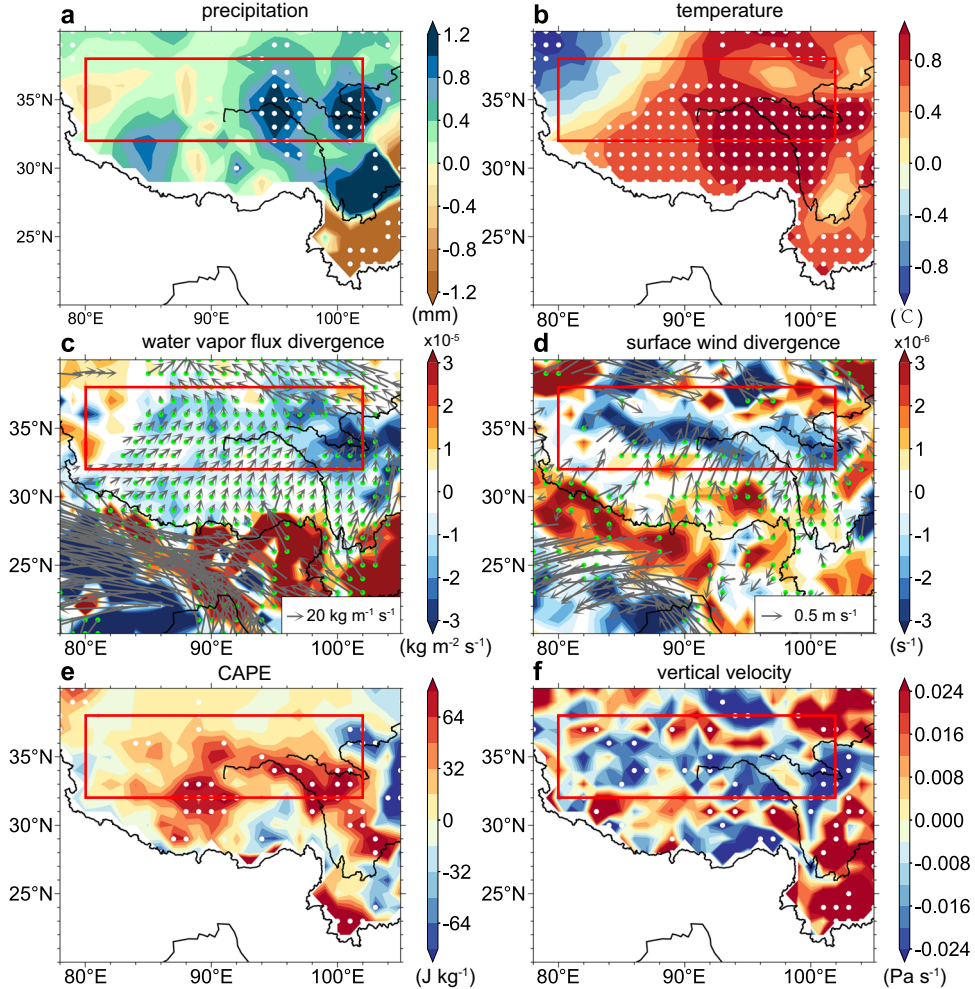


**Fig. 3 Composite differences in precipitation, temperature, energy and water vapor transport between the relatively warm period and relatively cold period during the regional CHTRE.** Differences in (a) precipitation (units: mm), (b) mean temperature (units: °C), (c) vertically integrated water vapor flux divergence (units:  $\text{kg m}^{-1} \text{s}^{-1}$ ), (d) surface wind divergence (units:  $\text{s}^{-1}$ ), (e) convective available potential energy (units:  $\text{J kg}^{-1}$ ) and (f) vertical velocity at 500 hPa (units:  $\text{Pa s}^{-1}$ ) between the relatively warm period (1988–2014) and the relatively cold period (1961–1987). The dotted area indicates that the differences are significant at the 90% confidence level. The vectors in (c) and (d) denote the differences in vertically integrated water vapor transport (units:  $\text{kg m}^{-2} \text{s}^{-1}$ ) and surface wind (units:  $\text{m s}^{-1}$ ), respectively, where the differences are significant at the 90% confidence level. The red rectangles denote western China ( $80\text{--}102^\circ\text{E}$ ,  $32\text{--}38^\circ\text{N}$ ).

and a large amount of water vapor can accumulate over western China. Therefore, as shown in Fig. 2, the water-holding capacity of the atmosphere has increased significantly in western China, so the total column water vapor increased significantly in western China (at the 95% confidence level).

In addition, the transient convective available potential energy is significantly increased during the relatively warm period (Fig. 3b, e), indicating that the atmospheric instability is increased, which leads to increased convergence of the near-surface winds (Fig. 3d) and enhanced convection in the atmosphere (Fig. 3f) over western China. In brief, the increased air temperature resulted in enhanced transient water vapor convergence and transient convective motion, which intensified the severity of CHTRE in western China (Fig. 3a, b).

### Model performance

In general, the accuracy of detection and attribution depends on the performance of a large number of climate models. To select the optimal simulations, the capabilities of the twelve CMIP6 models for the simulation of climatological spatial patterns of temperature and precipitation in China were evaluated based on Taylor analysis (see Methods). A good model simulation should

have three characteristics, i.e., the standard deviation and correlation are close to unity and the root mean square error (RMSE) is close to zero<sup>44</sup>.

As shown in Fig. 4a, b, most models can reproduce the climatological spatial pattern of mean temperature and total precipitation in the summers of 1961–2014. In particular, CanESM5 and MIROC6 have relatively poor capability in simulating the climatological spatial pattern of mean temperature, with relatively small spatial correlation coefficients of 0.89 and 0.893 between simulation and observation for CanESM5 and MIROC6, respectively (Supplementary Figure 3). For the climatology of total precipitation, the spatial correlation coefficients between the observed precipitation and simulations are approximately 0.8, and the RMSEs are smaller than 0.75 for all twelve models except FGOALS-g3, which shows a relatively poor performance with a spatial correlation coefficient of 0.53 and an RMSE of 0.77 (Fig. 4b). The differences in total precipitation between the simulations of CMIP6 models and observation indicate that the deviation mainly comes from the overestimation in the TP and underestimation in EC and SC (Supplementary Figure 4). When focusing on the mean temperature and total precipitation in summer, although the observed temperature and precipitation were within the range of

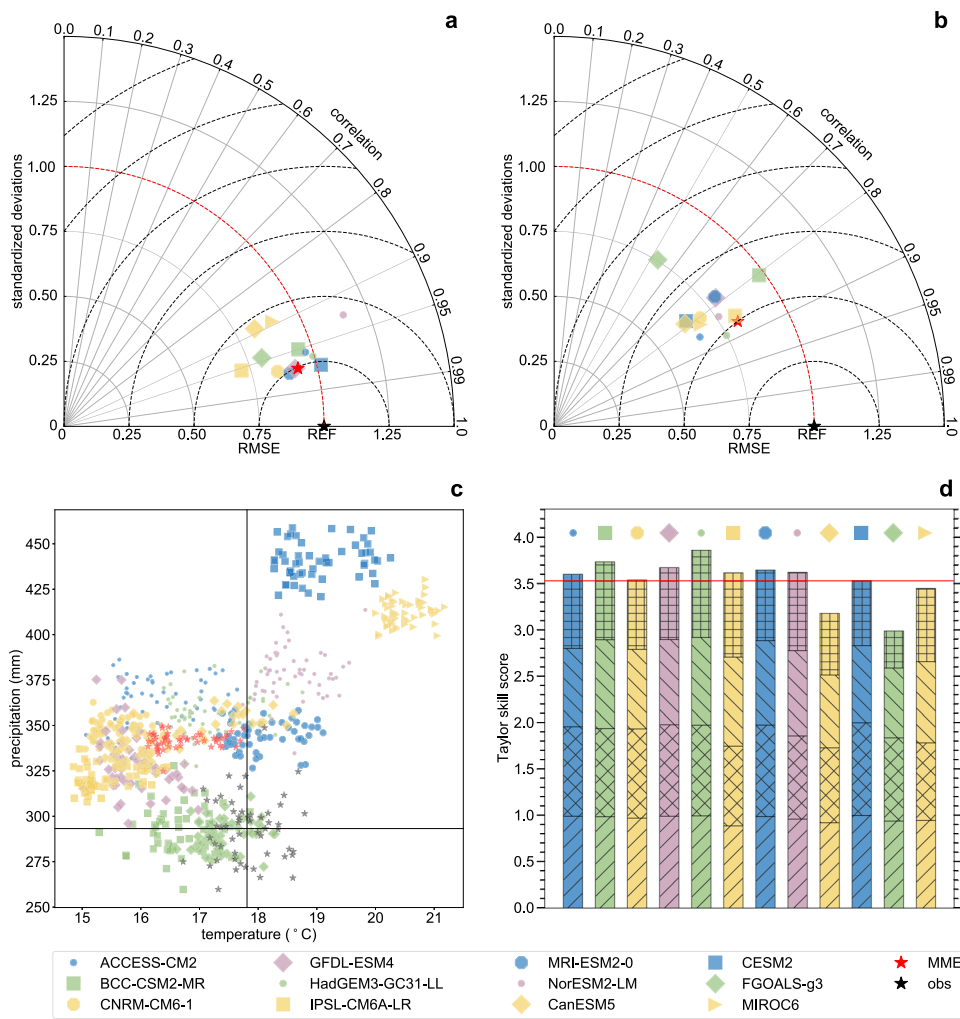


**Fig. 4 Taylor analysis of mean temperature and total precipitation in summer.** Taylor diagram showing the climatological spatial patterns of (a) mean temperature and (b) total precipitation. Scatter plot of (c) total precipitation vs. mean temperature in summer over China. Taylor skill score 1 (marks “/” and “\”) and Taylor skill score 2 (marks “x” and “+”) on (d) mean temperature and total precipitation of twelve models (represented by different colors and shapes above histogram) in summer over China, respectively. The black horizontal and vertical lines in (c) represent the average of the observed total precipitation and mean temperature, respectively. The red horizontal lines in (c) represent the average of Taylor skill score 1 and Taylor skill score 2 on both temperature and precipitation. Symbols with different colors and shapes represent simulations of different models and MME of the preferred model as well as observations.

one standard deviation of the twelve models (Supplementary Figure 5), the CESM2 and MIROC6 models significantly deviate from the observed mean temperature and total precipitation (Fig. 4c).

Overall, combined with the evaluation of the performance of the twelve models regarding regional summer average values and Taylor spatial skill scores (see Methods), four models, i.e., CanESM5, CESM2, FGOALS-g3 and MIROC6, show relatively poor skills (Fig. 4d, the Taylor spatial skill scores are lower than the comprehensive Taylor skill scores (ATS)), and their simulations are excluded from the study. The multimodel ensemble median (MME) of the remaining eight models, ACCESS-CM2, BCC-CSM2-MR, CNRM-CM6-1, GFDL-ESM4, HadGEM3-GC31-LL, IPSL-CM6A-LR, MRI-ESM2-0 and NorESM2-LM, were thus used for further analysis (Supplementary Table 1).

### Detection and attribution

Considering that the CHTDE and CHTRE in different regions of China have different long-term trends (Fig. 1) and the underlying reasons may be different, the following discussion focuses on the detection and attribution of CHTDE and CHTRE trends in five

subregions of China, NWC, TP, NEC, EC and SC, as shown in Fig. 1. Based on the simulations of the eight CMIP6 models, the linear trends of CHTDEI and CHTREI under different forcings were obtained (Fig. 5). As shown in Fig. 6, the downward trends of CHTDEI and CHTREI are  $-0.13$  and  $-0.07$ , respectively, indicating that the severity of observed CHTDE and CHTRE has significantly increased across China at the 95% confidence level. The results show that the observed intensification of CHTDE and CHTRE severity can be captured by CMIP6 models from historical all-forcing (hist-ALL) simulations in most areas of China (Fig. 5a, g).

Specifically, for CHTDE, the MME response to historical greenhouse gas forcing (hist-GHG) is similar to its response to historical anthropogenic forcing (hist-ANT), which is obtained by subtracting the historical natural forcing (hist-NAT) simulation from the hist-ALL simulation. The hist-ANT and hist-GHG simulations exhibit an intensifying severity of CHTDE (Fig. 5c, e), especially in NWC, TP and NEC (Fig. 6a). However, the spatial distribution of historical aerosol forcing (hist-AER) is likely to offset the decreasing trend of CHTDEI in the TP, EC and SC (Fig. 5b, Fig. 6a) and thus alleviate the intensification of CHTDE. It is worth noting that there is a significant upward trend in the severity of CHTDE under other

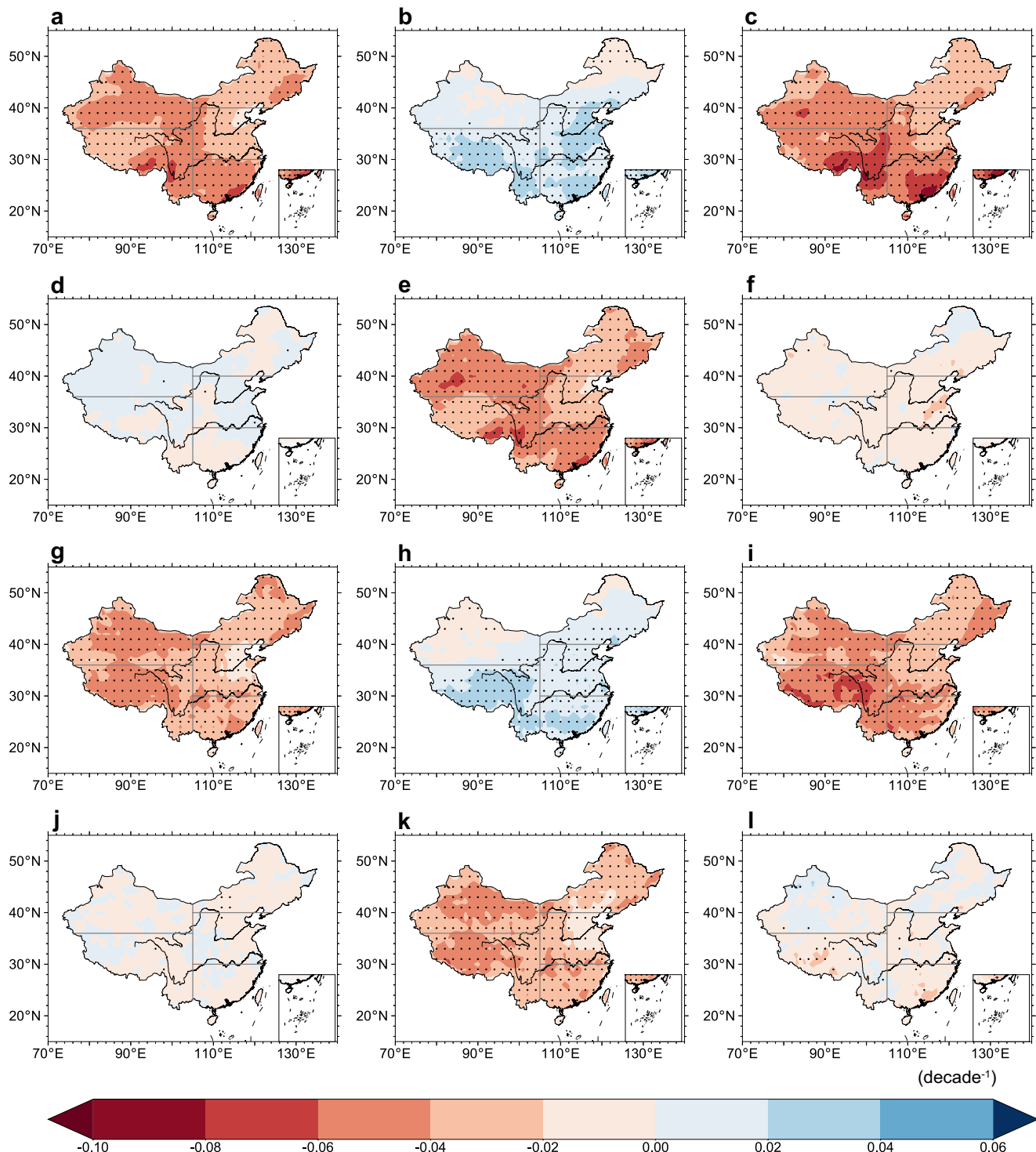


**Fig. 5 Linear trends of CHTDEI and CHTREI under different forcings.** Linear trends of (a–f) CHTDEI and (g–l) CHTREI in response to different forcings (a and g for historical all forcing; b and h for historical aerosol forcing; c and i for historical greenhouse gases forcing; d and j for historical natural forcing; e and k for historical anthropogenic forcing; f and l for historical other anthropogenic forcing) during the summers from 1961 to 2014 (units: decade<sup>-1</sup>) over China. The dotted area indicates that the linear trend is significant at the 95% confidence level.

historical anthropogenic forcings (historical other anthropogenic forcing (hist-OA), estimated by subtracting the response to hist-GHG and hist-NAT from hist-ALL<sup>45</sup>), including land use and ozone (Fig. 5f, Fig. 6a). External forcings may increase the severity of CHTRE under hist-ALL (Fig. 5g), hist-GHG (Fig. 5i) and hist-ANT (Fig. 5k) over China. Additionally, the result based on the MME of hist-AER shows an increasing trend of CHTREI in the TP and

eastern China, suggesting that aerosols are favorable for reducing the severity of CHTRE in TP (Fig. 5h, Fig. 6b).

Based on the above observations and external forcings of MME, the optimal fingerprint method<sup>46,47</sup> was used to quantify the influence of external forcings on the observed CHTDEI or CHTREI during 1961–2014 (see Methods and Supplementary Method 1). Single-signal analysis was used to detect the effects of different

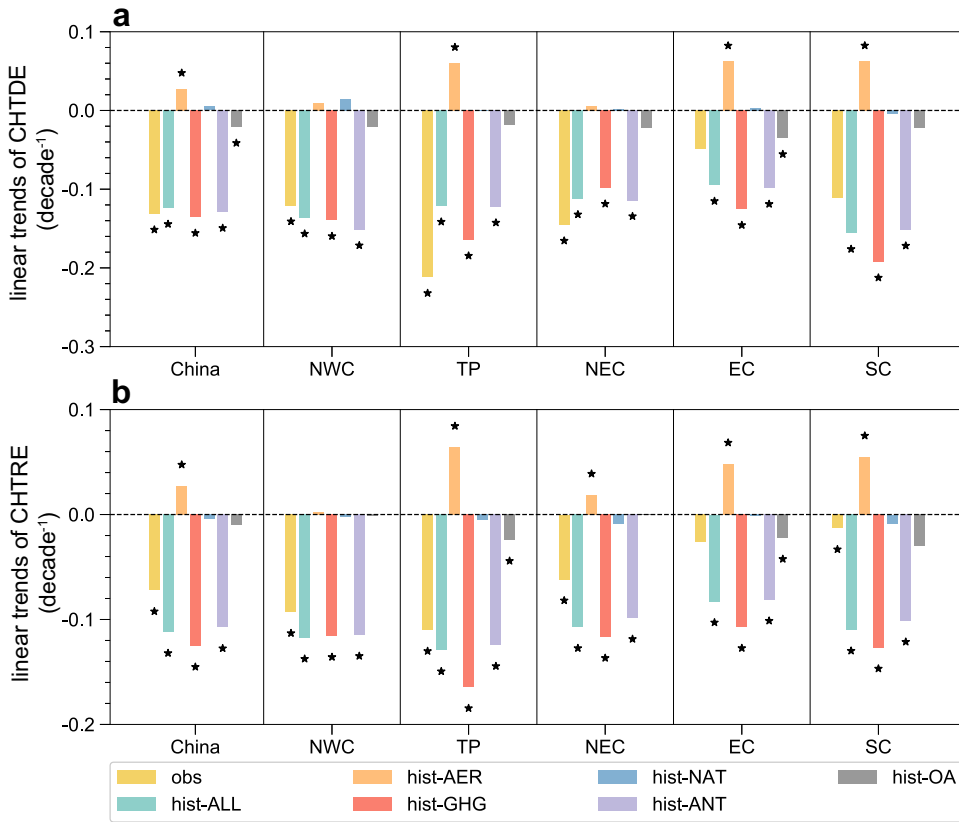


**Fig. 6 Linear trends of regional average CHTDEI and CHTREI from observations and simulations.** Regional average trends for nonoverlapping three-year mean (a) CHTDEI and (b) CHTREI from observations and MME under external forcing across China and in different subregions of China (units: decade<sup>-1</sup>). The asterisks denote that the trend is significant at the 95% confidence level.

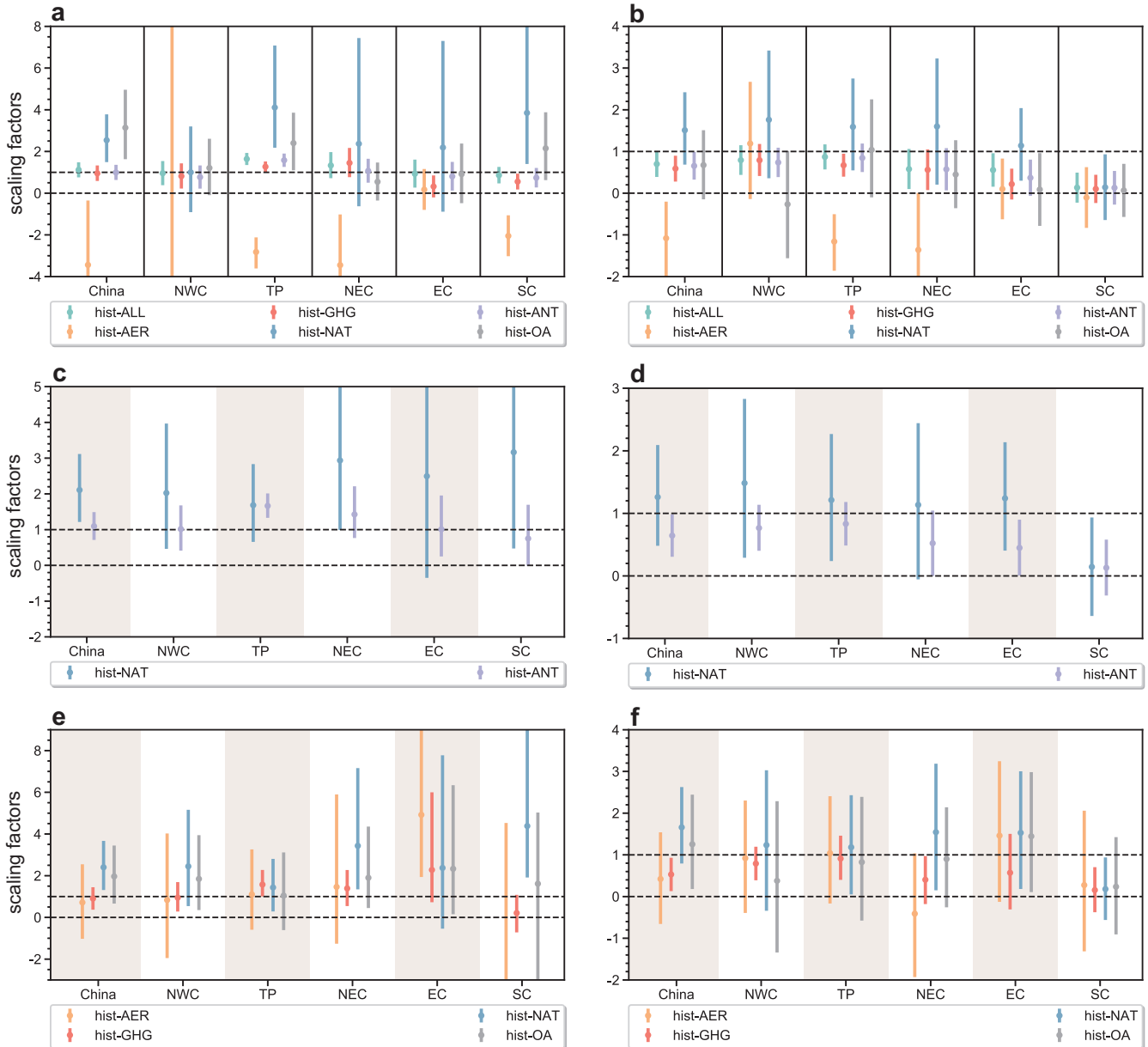
natural and anthropogenic forcings on the severity of CHTDE and CHTRE. To examine the relative contributions of anthropogenic activities and natural forcing and separate the hist-NAT and hist-ANT signals from each other<sup>48</sup>, two-signal analysis, which regresses observed CHTDEI/CHTREI onto hist-ANT and hist-NAT simultaneously, was applied for further analysis. Moreover, the observed CHTDEI/CHTREI were regressed onto hist-AER, hist-GHG, hist-OA and hist-NAT simultaneously by four-signal analysis to clarify the relative effects of various external anthropogenic forcings on the changes in CHTDE and CHTRE compared to the effects of natural forcing signals<sup>49,50</sup>.

Figure 7a presents the scaling factors obtained by regressing the time series of observed CHTDEI anomalies onto the MME response to a single forcing for the period of 1961–2014. Across China, the scaling factors for hist-ALL, hist-ANT, hist-GHG, hist-OA and hist-NAT are significantly greater than zero, suggesting that the effects of both anthropogenic forcing and natural forcing on CHTDE can be detected in China. For different subregions, the best estimates of scaling factors in hist-ANT and hist-GHG are very close to unity, indicating that the severity of CHTDE under anthropogenic external forcing, especially under hist-GHG, is in good agreement with the observed severity of CHTDE. Hist-OA can be detected in the TP and SC. Moreover, the scaling factor of hist-AER in the TP and SC is negative, which is consistent with the spatial pattern of the hist-AER trend. In addition to anthropogenic forcing, the scaling factors and 90% uncertainty ranges of hist-NAT in the TP and SC are greater than zero, but the uncertainty ranges are much larger than those under other forcings (Fig. 7a). In conclusion, the impacts of anthropogenic factors on the severity of CHTDE in most areas of China, particularly in NWC, TP, NEC and SC, can be detected. Hist-GHG is an important forcing for the change in the severity of CHTDE in China. In contrast, hist-AER can

reduce the severity of CHTDE in China, and this effect is most significant in the TP and SC.

For the scaling factors from the two-signal (Fig. 7c) and four-signal (Fig. 7e) analysis of CHTDEI, the residual consistency test indicates that all the results have reached the 90% confidence level, suggesting that the multisignal regression model fits the observed data well. It is clear that the signals of hist-ANT (two-signal analysis) and hist-GHG (four-signal analysis) can be regarded as the main external forcings that lead to changes in the severity of CHTDE in China. Furthermore, the signals of hist-OA and hist-NAT can also be detected robustly in multiple-signal analysis, which may be different from previous studies<sup>26,27</sup>. When focusing on each individual subregion in China, the impact of hist-ANT can be separated from that of hist-NAT to dominate the severity of CHTDE (the forcing signals can be considered attributable signals in single-signal analysis and can be successfully detected in multisignal analysis concurrently) in NWC, NEC, and SC. Hist-GHG can be separated from other forcings to dominate the severity of CHTDE in NWC, TP, and NEC. In general, hist-ANT and hist-GHG are the primary causes for the increasing severity of CHTDE, and they can be separated from other forcings to dominate the severity of CHTDE in China.

Similarly, Fig. 7b, d and f show the scaling factors of CHTREI from a single signal, two signals and four signals, respectively. Across China, the 90% confidence interval of the scaling factor under hist-NAT is greater than zero and includes unity, suggesting that the severity of CHTREI can be largely attributed to hist-NAT. In addition, hist-ANT and hist-GHG can be detected robustly. The scaling factor of hist-AER in China is negative, which suggests the offsetting role of hist-AER on the decreasing trend of the CHTREI. In terms of different subregions, changes in the severity of CHTREI in the TP can be attributed to both hist-ANT and hist-NAT. The



**Fig. 7 Detection and attribution analysis for the severity of CHTDE and CHTRE.** Best estimates of the scaling factors (dots) and their 5–95% uncertainty ranges (error bars) from (a, b) single-signal (hist-ALL, hist-AER, hist-GHG, hist-NAT, hist-ANT and hist-OA), (c, d) two-signal (hist-NAT and hist-ANT) and (e, f) four-signal (hist-AER, hist-GHG, hist-NAT, and hist-OA) analyses for (a, c, e) CHTDE and (b, d, f) CHTRE in different subregions and across China. The two dashed lines parallel to the horizontal axis represent zero and unity.

scaling factors of hist-ANT and hist-GHG are greater than zero and include unity in NWC, which means that both hist-ANT and hist-GHG can be separated from other forcings to dominate the increasing severity of CHTRE in NWC. Additionally, hist-ANT can dominate the increasing severity of CHTRE in NEC. However, according to the single-signal case, the detected signals for hist-ALL, hist-ANT and hist-GHG overestimated the observed change in CHTRE. Overall, both hist-ANT and hist-NAT are favorable for the increasing severity of CHTRE in China, particularly in western China, where the linear trend of the CHTREI changed significantly.

Finally, we quantified the changes in the severity of CHTDE and CHTRE attributed to different external forcings. Figure 8 shows the linear changes in the severity of CHTDE and CHTRE from 1961 to 2014, that is, the product of the linear trend of the CHTDEI/CHTREI and the corresponding time period, reflecting the linear changes in observed CHTDEI/CHTREI or attributable

to different forcings over the entire period from 1961 to 2014. Across China, the observed CHTDEI decreased by  $-0.24$  ( $-0.32$  to  $-0.16$ ) during 1961–2014 (Fig. 8a). The attributable change of hist-GHG to the observed CHTDEI is  $-0.22$  ( $-0.35$  to  $-0.09$ ) in China, which probably contributes 93% to the observed linear change in the severity of CHTDE. The contribution from hist-ANT is greater than 96% in different subregions. Moreover, for the attributable change of hist-AER is  $0.04$  ( $-0.06$  to  $0.12$ ), indicating that hist-AER partially offsets the decline in the CHTDEI by approximately 15%. Specifically, the CHTDEI decreases by  $-0.07$  ( $-0.13$  to  $-0.03$ ) for hist-OA, which contributes to the increased severity of CHTDE by approximately 32%. For CHTRE in Fig. 8b, the major decreases in CHTREI in TP and NWC are  $-0.20$  ( $-0.25$  to  $-0.14$ ) and  $-0.17$  ( $-0.21$  to  $-0.12$ ), respectively. The attributable linear changes in hist-GHG and hist-ANT exceed approximately 90% of the

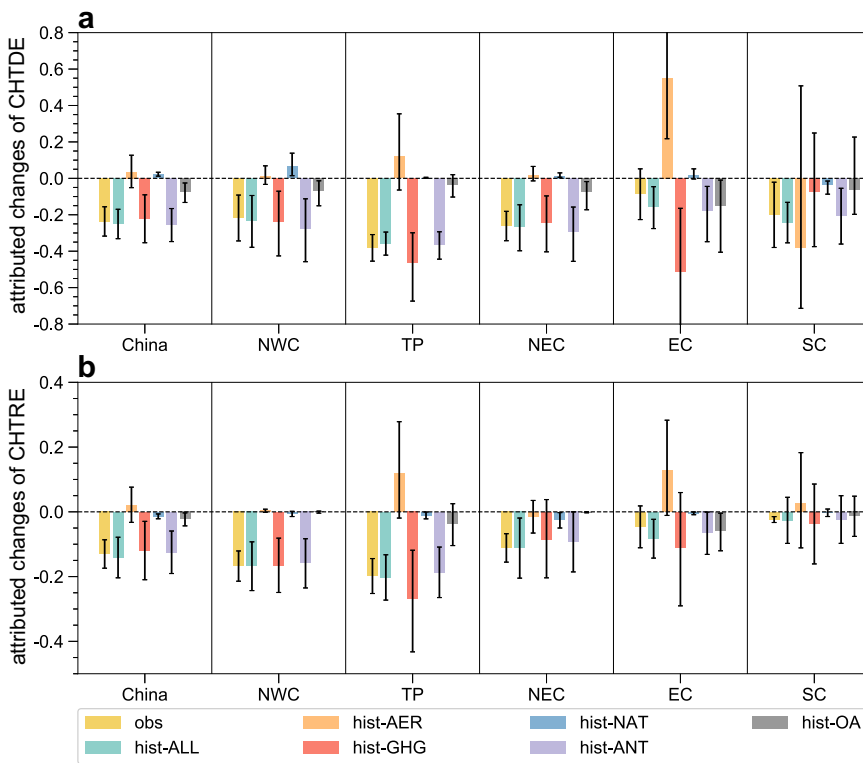


**Fig. 8 Attributed linear changes in the severity of CHTDE and CHTRE during 1961–2014.** Estimates of observed linear changes in the severity of (a) CHTDE and (b) CHTRE and the corresponding total attributed linear changes in response to different external forcings based on the original change. The attributable linear changes are calculated by the trends for the MME of the CHTDEI and CHTREI time series. Additionally, the observed changes in the CHTDEI and CHTREI are estimated by the trend multiplied by the corresponding time period. The error bars indicate the 5–95% uncertainty range, while the 90% uncertainty range is calculated by the total least square method. The scaling factors used to constrain the attributable changes are derived by single-signal forcing for hist-ALL, two-signal forcing for hist-ANT and four-signal forcing for hist-AER, hist-GHG, hist-NAT and hist-OA.

observed change in CHTRE severity in China. CHTREI is estimated to decrease by  $-0.12$  ( $-0.19$  to  $-0.06$ ) for hist-ANT, which accounts for 95% of the increasing severity of CHTRE across China. This illustrates that anthropogenic climate change is more important for the linear change in the increasing severity of compound extreme events across China. However, the linear change in hist-AER plays a role in reducing the severity of CHTDE and CHTRE, especially in the TP.

## DISCUSSION

In this study, the relative threshold counting method and Archimedes copulas method are used to establish an index to characterize the severity of CHTDE and CHTRE. The underlying mechanism for the changes in the severity of CHTDE and CHTRE over China under global warming is explored. To quantify the influence of global warming on the changes in CHTDE and CHTRE, detection and attribution analysis of the severity of CHTDE and CHTRE in the summers from 1961 to 2014 was carried out based on CMIP6 models that simulate temperature and precipitation well in China.

The results indicate that the severity of CHTDE shows a significant increasing trend in most areas of China. In addition, the severity of CHTRE has increased in China, particularly in Western China. The quantitative optimal fingerprint method shows that the change in the severity of CHTDE over China can be largely attributed to hist-ANT, especially hist-GHG, which produces more than 90% of the attributable contribution to the observed CHTDE. In contrast, the signal of hist-NAT with large uncertainty can be robustly detected in the change in CHTRE,

particularly in western China. However, the contribution of anthropogenic forcing to the linear change in the severity of CHTRE is still over 90%.

The variation in natural forcing is closely related to the variability in extreme events. Natural forcing can affect the variation in extreme events by changing the atmospheric circulation in middle and high latitudes. For example, extreme precipitation decreases significantly in the monsoon region after volcanic eruptions<sup>51</sup>. According to the original time series of CHTDEI and CHTREI, the long-term trends under hist-ANT and hist-GHG are basically consistent with that of observations, and the observed interannual-to-decadal variability in the CHTREI is characterized by a 10-year quasiperiodic oscillation that is similar to the CHTREI forced by hist-NAT (Supplementary Figure 6, Supplementary Figure 7). To reduce the multitime scale variation and identify the main sources of long-term trends, the original time series of CHTDEI and CHTREI are decomposed into nonlinear trends and interannual-to-decadal variability by the ensemble empirical mode decomposition method<sup>52</sup> (Supplementary Method 2, Supplementary Figure 8 and Supplementary Figure 9). The 90% confidence intervals of the nonlinear trends on CHTDEI and CHTREI of hist-GHG and hist-ANT are significantly reduced compared with the original time series, confirming with high confidence that anthropogenic forcing is the dominant factor of the linear trend on the severity of CHTDE and CHTRE (Supplementary Figure 10, Supplementary Figure 11). This illustrated that hist-NAT, which was not detected, may be linked to the interannual-to-decadal variability in the severity of compound extreme events over China. This will be further studied in the future. In brief, consistent with many existing studies, we verify the

fact that compound extreme events are increasing under global warming<sup>53–55</sup>. We emphasize and quantify the contribution of human activities to intensified compound extreme events on smaller regional scales, highlighting the regional differences in the drivers of compound events. However, it is significant that there are some deviations in CMIP6 data, especially in the regional precipitation data<sup>56</sup>. Therefore, it is necessary to adopt other effective methods and accurate regional climate model data to improve and verify the results.

In addition, the interaction of meteorological factors and human activities can intensify the occurrence of extreme events<sup>57</sup>. For example, the increasing probability of a double jet affects long waves in mid-latitudes, forming stable weather conditions and promoting the formation of heat waves<sup>58</sup>. We found that the increased water-holding capacity of the atmosphere and decreased relative humidity under global warming are important reasons for the increasing severity of CHTDE over China, especially in the TP. For the intensified severity of CHTRE, the enhanced transient water vapor transport from the Bay of Bengal and enhanced transient convective available potential energy in western China intensified the severity of regional CHTRE under the interaction of transient dynamic lifting and transient water vapor convergence. The limited MME of the eight models used cannot reproduce the historical change in relative humidity (Supplementary Figure 12); thus, it is difficult to explore the contribution of meteorological factors to the increased severity of CHTDE and CHTRE under global warming. In the future, the different roles of different meteorological factors in mediating the influence of human activities on the intensity of compound events should be analyzed. Additionally, further studies are necessary to investigate the changes in CHTDE and CHTRE under different scenarios in the future based on more advanced cross-disciplinary methods<sup>59</sup>.

## METHODS

### Definitions of the CHTDE index (CHTDEI) and CHTRE index (CHTREI)

To quantify the severity of compound events, CHTDEI and CHTREI are defined as the combined probability of the number of days and maximum duration of the simultaneous occurrence of high temperature and drought (rain) events. First, the concurrence of daily temperature greater than the 90<sup>th</sup> percentile and daily total precipitation greater than the 75<sup>th</sup> percentile (less than 25<sup>th</sup> percentile) in the summers (June, July and August) of 1961–2014 is defined as a CHTRE (CHTDE).

Second, the number of days (the total number of CHTDE/CHTRE) and maximum duration (maximum number of consecutive days in summer when CHTDE/CHTRE occurred) in each summer are taken as random variables  $X$  and  $Y$  with marginal distributions as shown in Eq. (2) and Eq. (3), respectively.

$$F_X(x) = P(X \leq x) \quad (2)$$

$$F_Y(y) = P(Y \leq y) \quad (3)$$

To avoid making assumptions about variable distribution types, the empirical Gringorten plotting formula

$$P(x_i) = \frac{m_i - 0.44}{n + 0.12} \quad (4)$$

is used to estimate marginal probability distribution functions of days and duration with empirical distribution, while  $n$  is sample size and  $m_i$  is the number of  $x_t \leq x_i (1 \leq t \leq n)$ .

Finally, based on the number of days and maximum duration of CHTDE and CHTRE, the bivariate copula

$$F(x, y) = P(X \leq x, Y \leq y) = C(F_X(x), F_Y(y); \theta) \quad (5)$$

is used to construct the severity index

$$\text{PI} = P(X > x, Y > y) = 1 - F_X(x) - F_Y(y) + C(F_X(x), F_Y(y)) \quad (6)$$

of compound extreme events. The three widely accepted Archimedean copulas (Supplementary Note 1) are applied in this study<sup>14,60,61</sup>. A smaller severity index (PI) represents a smaller joint probability of more frequent (greater than  $x$ ) and longer duration (greater than  $y$ ) compound events, indicating that the potential CHTDE (CHTRE) is more severe. For convenience, the PIs for CHTDE and CHTRE are called CHTDEI and CHTREI, respectively.

### Evaluation method of the copula model

To determine the optimal fitting copulas for calculating multivariate joint distribution, we use three criteria to compare the performance of different copulas, including the Akaike Information Criterion (AIC) information criterion method, the Bayesian Information Criterion (BIC) rule method and the Root Mean Square Error (RMSE) criterion. These criteria are based on the empirical joint distribution of observed sample points<sup>36</sup>. More specifically, the empirical joint distribution is expressed as

$$F(x_i, y_i) = P(x \leq x_i, y \leq y_i) = \frac{\sum_{l=1}^i \sum_{k=1}^i N_{lk} - 0.44}{n + 0.12} \quad (7)$$

Where  $N_{lk}$  is the number of  $x \leq x_i$  and  $y \leq y_i$  in the joint observation samples of size  $n$ .

The AIC information criterion method considers both the overregulation due to the complexity of the model and minimization of error residuals, which is a relatively robust indicator to measure the model effect. The formula is written as:

$$\text{MSE} = \frac{1}{n} \sum_{i=1}^n (F(x_i, y_i) - C(u_i, v_i))^2 \quad (8)$$

$$\text{AIC} = n \ln \text{MSE} + 2m \quad (9)$$

where  $m$  is the number of copula model parameters. Similar to the AIC, the BIC is expressed as follows:

$$\text{BIC} = n \ln \text{MSE} + m \ln n \quad (10)$$

In addition,

$$\text{RMSE} = \sqrt{\frac{1}{n} \sum_{i=1}^n (F(x_i, y_i) - C(u_i, v_i))^2} \quad (11)$$

is also used in this study. More importantly, a lower AIC, BIC and RMSE are associated with a better fit of the copula model. The evaluation results are shown in Supplementary Table 2 and Supplementary Table 3. The Clayton copula and Gumbel copula performed optimally for the CHTDEI and CHTREI, respectively.

### Linear trend

The linear trend estimation (unitary linear regression) method is used to calculate the trend slopes. If  $x_i$  is used to represent the sample point whose sample size is  $n$ ,  $t_i$  is used to represent the time corresponding to  $x_i$ . Then, a linear regression equation of one

variable between  $x_i$  and  $t_i$  is established as follows:

$$x_i = a + bt_i \quad i = 1, 2, \dots, n \quad (12)$$

$$b = \frac{\sum_{i=1}^n x_i t_i - \frac{1}{n} \left( \sum_{i=1}^n x_i \right) \left( \sum_{i=1}^n t_i \right)}{\sum_{i=1}^n t_i^2 - \frac{1}{n} \left( \sum_{i=1}^n t_i \right)^2} \quad (13)$$

$$a = \bar{x} - b\bar{t} \quad (14)$$

The coefficients were determined by the least squares method. Regression coefficient  $b$  represents the variable trend (sample  $x_i$ ). If the sign of  $b$  is positive, the variable shows an upward trend with increasing time  $t$ . Otherwise, it shows a downward trend. Since  $b$  represents the overall increase or decrease in the sample per year, multiplying by 10 represents the change in the sample per decade.

## Spatial correlation analysis

The Pearson correlation coefficient (Pearson product-moment correlation coefficient)

$$R = \frac{\sum_{i=1}^n (x_i - \bar{x})(y_i - \bar{y})}{\sqrt{\sum_{i=1}^n (x_i - \bar{x})^2 \sum_{i=1}^n (y_i - \bar{y})^2}} \quad (15)$$

is used to analyze the correlation between the observations and model simulations in Taylor analysis<sup>44</sup>. Here,  $n$  is the sample size, and  $x_i$  and  $y_i$  are observations and model simulation values for the  $i^{\text{th}}$  grid;  $\bar{x}$  and  $\bar{y}$  are the modeled and observed averages of all grid points, respectively.  $R$  presents the correlation coefficient with a value between  $-1$  and  $1$ . A positive  $R$  value denotes a positive correlation, and vice versa. A larger absolute  $R$  value denotes a larger correlation.

## Taylor spatial skill score rules

To select better models quantitatively, a comprehensive Taylor skill score ATS is defined using

$$S_1 = \frac{4(1+R)}{\left(\hat{\sigma}_f + \frac{1}{\hat{\sigma}_f}\right)^2 (1+R_0)} \quad (16)$$

$$S_2 = \frac{4(1+R)^4}{\left(\hat{\sigma}_f + \frac{1}{\hat{\sigma}_f}\right)^2 (1+R_0)^4} \quad (17)$$

as proposed by Talyer<sup>44</sup>. Here,  $R$  represents the spatial correlation between observations and model simulations,  $R_0$  represents the maximum value of  $R$  in the twelve selected models, and  $\hat{\sigma}_f$  represents the ratio of the model standard deviation to the observed standard deviation.  $S_{1t}$  and  $S_{2t}$  are spatial skill scores of the models on climatological spatial distribution of temperature based on  $S_1$  and  $S_2$ , respectively.  $S_{1p}$  and  $S_{2p}$  are the spatial skills of the models on the climatological spatial distribution of total summer precipitation based on  $S_1$  and  $S_2$ , respectively. The total skill score is

$$S = S_{1t} + S_{2t} + S_{1p} + S_{2p} \quad (18)$$

Therefore, the average skill score of the twelve models is

$$\text{ATS} = \frac{1}{12} \sum_{i=1}^{12} S_i. \quad (19)$$

If the total skill score  $S$  of the  $i^{\text{th}}$  model is higher than ATS, the model performance of the  $i^{\text{th}}$  model is considered to be better. Otherwise, it is considered to be poor and will be removed.

## Optimal fingerprint method

In this study, the optimal fingerprint method<sup>46,47</sup> is applied for detection and attribution in CHTDE and CHTRE. To perform full-ranked estimation of internal covariance and avoid using empirical orthogonal function truncation, the regularized optimal fingerprint method based on the total least squares is applied to quantify the consistency between the model-simulated responses of CHTDE and CHTRE and observations in China (see Supplementary Method 1). The key information of the optimal fingerprint method is the scaling factor  $\beta_i$ , which quantifies the amplitude of the external forcing response to the observation. If the probability of observed change that occurs randomly due to the internal variability is smaller than 10%, it is called detection; that is, the 90% (5%-95%) confidence interval of the scaling factor is greater than zero. If the 5%-95% margin of the scaling factor is greater than zero and includes unity, it can further confirm the most likely cause of detected changes in CHTDE and CHTRE at a certain confidence level, which is called attribution.

To quantify the contribution of different external forcings to the severity of CHTDE and CHTRE in the observations, the attributable contribution rate can be expressed as:

$$\text{Contribution Rate}_i = \frac{\Delta \text{PI}_i}{\Delta \text{PI}_{\text{obs}}} \times 100\% \quad (20)$$

where  $\Delta \text{PI}_i$  is the attributable changes in the CHTDEI and CHTREI caused by external forcing  $i$ , which is obtained by multiplying the linear trend from the data modified by the CHTDEI and CHTREI simulated by external forcing  $i$  by the best estimate of the corresponding best estimate of the scaling factor (5%-95% margin of scaling factor) multiplied by the time period of the time series. The observed change  $\Delta \text{PI}_{\text{obs}}$  is calculated by multiplying the observed CHTDEI and CHTREI trends (90% uncertainty range) by the corresponding time period.

## DATA AVAILABILITY

The temperature, precipitation and relative humidity derived from the CN05.1 observation datasets ("CN" represents the domain of China; "05" represents the horizontal resolution of  $0.5^{\circ} \times 0.5^{\circ}$ ; ".1" represents the advanced version of CN05) are available at <https://ccrc.iap.ac.cn/resource>. CN05.1 datasets are high-quality observational daily data on  $0.25^{\circ} \times 0.25^{\circ}$  grids, which are constructed based on measurements collected at more than 2400 national observation stations in China. The CMIP6 daily temperature and precipitation datasets from preindustrial unforced control simulation experiments, historical all forcing (hist-ALL) experiments and the different external forcing experiments (including historical natural forcing hist-NAT, historical aerosol forcing hist-AER and historical greenhouse gas forcing hist-GHG) of the Detection and Attribution Model Intercomparison Project are available at <https://esgf-node.llnl.gov/search/cmip6/>. The ERA5 reanalysis datasets (including total column water vapor, vertical integral of water vapor flux, surface wind, vertical velocity and convective available potential energy) are available at <https://cds.climate.copernicus.eu/cdsapp#!/search?type=dataset>. The ERA5 daily data are obtained from the averaged 24 hourly data. For convenience, both the observational data and multimodel simulation data are remapped to  $1^{\circ} \times 1^{\circ}$  grids using the bilinear interpolation algorithm. The datasets generated during and/or analyzed during the current study are available from the corresponding authors on reasonable request.

## CODE AVAILABILITY

The code to carry out the current analyses is available from the corresponding authors upon request.

Received: 11 December 2022; Accepted: 27 June 2023;

Published online: 07 July 2023

## REFERENCES

- Coumou, D. & Rahmstorf, S. A decade of weather extremes. *Nat. Clim. Chang.* **2**, 491–496 (2012).
- Fischer, E. M., Sippel, S. & Knutti, R. Increasing probability of record-shattering climate extremes. *Nat. Clim. Chang.* **11**, 689–695 (2021).

3. Climate Change 2021. *The Physical Science Basis. Working Group I Contribution to the Intergovernmental Panel on Climate Change Sixth Assessment Report*. (Cambridge, United Kingdom and New York: Cambridge University Press, 2021).
4. Zhou, B. & Qian, J. Changes of weather and climate extremes in the IPCC AR6 (in Chinese). *Clim. Chang. Res.* **17**, 713–718 (2021).
5. Ministry of Emergency Management of the People's Republic of China. (2022). Available at: [https://www.mem.gov.cn/xw/yjglbgzdt/202209/t20220917\\_422674.shtml](https://www.mem.gov.cn/xw/yjglbgzdt/202209/t20220917_422674.shtml). (Accessed: 10th June 2023).
6. Liang, X. Extreme rainfall slows the global economy. *Nature* **601**, 193–194 (2022).
7. Cai, W. et al. The 2021 China report of the Lancet Countdown on health and climate change: seizing the window of opportunity. *Lancet Public. Health* **6**, e932–e947 (2021).
8. Mukherjee, S. & Mishra, A. K. Increase in compound drought and heatwaves in a warming world. *Geophys. Res. Lett.* **48**, 741–757 (2021).
9. Hao, Y. et al. Probabilistic assessments of the impacts of compound dry and hot events on global vegetation during growing seasons. *Environ. Res. Lett.* **16**, 074055 (2021).
10. Zhang, W. et al. Compound hydrometeorological extremes: drivers, mechanisms and methods. *Front. Earth. Sci.* **9**, 673495 (2021).
11. Managing the Risks of Extreme Events and Disasters to Advance Climate Change Adaptation. Field, C. B. et al. (eds.). *A Special Report of Working Groups I and II of the Intergovernmental Panel on Climate Change*. (Cambridge, United Kingdom and New York: Cambridge University Press, 2012).
12. Zscheischler, J. et al. A typology of compound weather and climate events. *Nat. Rev. Earth. Environ.* **1**, 333–347 (2020).
13. Leonard, M. et al. A compound event framework for understanding extreme impacts. *Wiley Interdiscip. Rev. Clim. Change* **5**, 113–128 (2014).
14. Zscheischler, J. & Seneviratne, S. I. Dependence of drivers affects risks associated with compound events. *Sci. Adv.* **3**, e1700263 (2017).
15. Bevacqua, E., Zappa, G., Lehner, F. & Zscheischler, J. Precipitation trends determine future occurrences of compound hot-dry events. *Nat. Clim. Chang.* **12**, 350–355 (2022).
16. Tencer, B., Weaver, A. & Zwiers, F. Joint occurrence of daily temperature and precipitation extreme events over Canada. *J. Appl. Meteorol. Climatol.* **53**, 2148–2162 (2014).
17. Xiao, X., Huang, D. & Yan, P. The climatic characteristics of compound extreme events (in Chinese). *J. Meteorol. Sci.* **40**, 744–751 (2020).
18. Wang, W., Zhang, Y., Guo, B., Ji, M. & Xu, Y. Compound droughts and heat waves over the Huai River Basin of China: From a perspective of the magnitude index. *J. Hydrometeorol.* **22**, 3107–3119 (2021).
19. Yu, R. & Zhai, P. More frequent and widespread persistent compound drought and heat event observed in China. *Sci. Rep.* **10**, 1–7 (2020).
20. Yu, R. & Zhai, P. Changes in compound drought and hot extreme events in summer over populated eastern China. *Weather. Clim. Extremes.* **30**, 100295 (2020).
21. Salvadori, G. & De Michele, C. Multivariate multiparameter extreme value models and return periods: A copula approach. *Water Resour. Res.* **46**, W10501 (2010).
22. Sarhadi, A., Ausin, M. C., Wiper, M. P., Touma, D. & Diffenbaugh, N. S. Multidimensional risk in a nonstationary climate: Joint probability of increasingly severe warm and dry conditions. *Sci. Adv.* **4**, eaau3487 (2018).
23. Hao, Z., Hao, F., Singh, V. P. & Zhang, X. Statistical prediction of the severity of compound dry-hot events based on El Niño-Southern Oscillation. *J. Hydrol.* **572**, 243–250 (2019).
24. Yu, R. & Zhai, P. Advances in scientific understanding on compound extreme events (in Chinese). *Trans. Atmos. Sci.* **44**, 645–649 (2021).
25. Wang, R., Lü, G., Ning, L., Yuan, L. & Li, L. Likelihood of compound dry and hot extremes increased with stronger dependence during warm seasons. *Atmos. Res.* **260**, 105692 (2021).
26. Chen, H. & Sun, J. Anthropogenic warming has caused hot droughts more frequently in China. *J. Hydrol.* **544**, 306–318 (2017).
27. Li, H., Chen, H., Sun, B., Wang, H. & Sun, J. A detectable anthropogenic shift toward intensified summer hot drought events over northeastern China. *Earth. Space Sci.* **7**, e2019EA000836 (2020).
28. Li, W., Jiang, Z., Li, L. Z., Luo, J. J. & Zhai, P. Detection and attribution of changes in summer compound hot and dry events over northeastern China with CMIP6 models. *J. Meteorol. Res.* **36**, 1–12 (2022).
29. Li, Y., Ding, Y. & Liu, Y. Mechanisms for regional compound hot extremes in the mid-lower reaches of the Yangtze River. *Int. J. Climatol.* **41**, 1292–1304 (2021).
30. Liu, Z. & Zhou, W. The 2019 autumn hot drought over the middle-lower reaches of the Yangtze River in China: Early propagation, process evolution, and concurrence. *J. Geophys. Res. Atmos.* **126**, e2020JD033742 (2021).
31. Chen, Y., Liao, Z., Shi, Y., Tian, Y. & Zhai, P. Detectable increases in sequential flood-heatwave events across China during 1961–2018. *Geophys. Res. Lett.* **48**, e2021GL092549 (2021).
32. Fischer, E. M. & Knutti, R. Anthropogenic contribution to global occurrence of heavy-precipitation and high-temperature extremes. *Nat. Clim. Chang.* **5**, 560–564 (2015).
33. Madakumbura, G. D., Thackeray, C. W., Norris, J., Goldenson, N. & Hall, A. Anthropogenic influence on extreme precipitation over global land areas seen in multiple observational datasets. *Nat. Commun.* **12**, 1–9 (2021).
34. Zscheischler, J. & Lehner, F. Attributing compound events to anthropogenic climate change. *Bull. Am. Meteorol. Soc.* **103**, E936–E953 (2022).
35. Alizadeh, M. R. et al. A century of observations reveals increasing likelihood of continental-scale compound dry-hot extremes. *Sci. Adv.* **6**, eaaz4571 (2020).
36. Sadegh, M., Ragno, E. & AghaKouchak, A. Multivariate Copula Analysis Toolbox (McCAT): Describing dependence and underlying uncertainty using a Bayesian framework. *Water Resour. Res.* **53**, 5166–5183 (2017).
37. Willmott, C. J. Some Comments on the Evaluation of Model Performance. *Bull. Am. Meteorol. Soc.* **63**, 1309–1313 (1982).
38. Wei, K. & Wang, L. Reexamination of the aridity conditions in arid northwestern China for the last decade. *J. Clim.* **26**, 9594–9602 (2013).
39. Trenberth, K. E. Atmospheric moisture residence times and cycling: Implications for rainfall rates and climate change. *Clim. Change* **39**, 667–694 (1998).
40. Ficklin, D. L. & Novick, K. A. Historic and projected changes in vapor pressure deficit suggest a continental-scale drying of the United States atmosphere. *J. Geophys. Res. Atmos.* **122**, 2061–2079 (2017).
41. Krishna, K. M. Intensifying tropical cyclones over the North Indian Ocean during summer monsoon—Global warming. *Glob. Planet. Change* **65**, 12–16 (2009).
42. Yang, J. et al. South Asian black carbon is threatening the water sustainability of the Asian Water Tower. *Nat. Commun.* **13**, 7360 (2022).
43. Berg, P., Moseley, C. & Haerter, J. O. Strong increase in convective precipitation in response to higher temperatures. *Nat. Geosci.* **6**, 181–185 (2013).
44. Taylor, K. E. Summarizing multiple aspects of model performance in a single diagram. *J. Geophys. Res. Atmos.* **106**, 7183–7192 (2001).
45. Najafi, M. R., Zwiers, F. W. & Gillett, N. P. Attribution of Arctic temperature change to greenhouse-gas and aerosol influences. *Nat. Clim. Chang.* **5**, 246–249 (2015).
46. Ribes, A., Planton, S. & Terray, L. Application of regularised optimal fingerprinting to attribution. Part I: method, properties and idealised analysis. *Clim. Dyn.* **41**, 2817–2836 (2013).
47. Ribes, A. & Terray, L. Application of regularised optimal fingerprinting to attribution. Part II: application to global near-surface temperature. *Clim. Dyn.* **41**, 2837–2853 (2013).
48. Sun, Y. et al. Rapid increase in the risk of extreme summer heat in Eastern China. *Nat. Clim. Chang.* **4**, 1082–1085 (2014).
49. Ma, S. et al. Detectable anthropogenic shift toward heavy precipitation over eastern China. *J. Clim.* **30**, 1381–1396 (2017).
50. Sun, Y. et al. Understanding human influence on climate change in China. *Natl. Sci. Rev.* **9**, 128–143 (2022).
51. Paik, S. & Min, S. K. Assessing the impact of volcanic eruptions on climate extremes using CMIP5 models. *J. Clim.* **31**, 5333–5349 (2018).
52. Wu, Z. & Huang, N. Ensemble empirical mode decomposition: a noise-assisted data analysis method. *Adv. Adapt. Data. Anal.* **1**, 1–41 (2009).
53. Wu, Y. et al. Global observations and CMIP6 simulations of compound extremes of monthly temperature and precipitation. *GeoHealth* **5**, e2021GH000390 (2021).
54. Hao, Z., Hao, F., Singh, V. P. & Zhang, X. Changes in the severity of compound drought and hot extremes over global land areas. *Environ. Res. Lett.* **13**, 124022 (2018).
55. Ridder, N. N., Pitman, A. J. & Ukkola, A. M. Do CMIP6 climate models simulate global or regional compound events skillfully? *Geophys. Res. Lett.* **48**, e2020GL091152 (2021).
56. Yazdandoost, F., Moradian, S., Izadi, A. & Aghakouchak, A. Evaluation of CMIP6 precipitation simulations across different climatic zones: Uncertainty and model intercomparison. *Atmos. Res.* **250**, 105369 (2021).
57. Bartusek, S., Kornhuber, K. & Ting, M. 2021 North American heatwave amplified by climate change-driven nonlinear interactions. *Nat. Clim. Chang.* **12**, 1–8 (2022).
58. Rousi, E., Kornhuber, K., Beobide-Arsuaga, G., Luo, F. & Coumou, D. Accelerated western European heatwave trends linked to more-persistent double jets over Eurasia. *Nat. Commun.* **13**, 3851 (2022).
59. Messori, G. et al. Compound climate events and extremes in the mid-latitudes: dynamics, simulation and statistical characterisation. *Bull. Am. Meteorol. Soc.* **102**, 1–13 (2020).
60. Genest, C. & MacKay, R. J. Copules archimédiennes et familles de lois bidimensionnelles dont les marges sont données. *Can. J. Stat.* **14**, 145–159 (1986).
61. Genest, C. & MacKay, R. J. The joy of copulas: Bivariate distributions with uniform marginals. *Am. Stat.* **40**, 280–283 (1986).

## ACKNOWLEDGEMENTS

This work was supported by the National Natural Science Foundation of China (grant 41991283), the National Key Research and Development Program of China (grant 2022FF0801704), the National Natural Science Foundation of China (grant 42005015), and the Postgraduate Research & Practice Innovation Program of Jiangsu Province (grant KYCX22\_1165).

## AUTHOR CONTRIBUTIONS

B.S. and W.L. contributed to the conception of the study. W.L. and B.S. analyzed and interpreted the data. W.L. and B.S. wrote the manuscript. H.W., B.Z., H.L., R.X. and M.D. helped to edit the manuscript. X.L. and W.A. offered suggestions for revision.

## COMPETING INTERESTS

The authors declare no competing interests.

## ADDITIONAL INFORMATION

**Supplementary information** The online version contains supplementary material available at <https://doi.org/10.1038/s41612-023-00413-3>.

**Correspondence** and requests for materials should be addressed to Bo Sun.

**Reprints and permission information** is available at <http://www.nature.com/reprints>

**Publisher's note** Springer Nature remains neutral with regard to jurisdictional claims in published maps and institutional affiliations.



**Open Access** This article is licensed under a Creative Commons Attribution 4.0 International License, which permits use, sharing, adaptation, distribution and reproduction in any medium or format, as long as you give appropriate credit to the original author(s) and the source, provide a link to the Creative Commons license, and indicate if changes were made. The images or other third party material in this article are included in the article's Creative Commons license, unless indicated otherwise in a credit line to the material. If material is not included in the article's Creative Commons license and your intended use is not permitted by statutory regulation or exceeds the permitted use, you will need to obtain permission directly from the copyright holder. To view a copy of this license, visit <http://creativecommons.org/licenses/by/4.0/>.

© The Author(s) 2023